

Supporting Information

High-Performance One-Dimensional Halide Perovskite Crossbar Memristors and Synapses for Neuromorphic Computing

Sujaya Kumar Vishwanath^{1*}, Benny Febriansyah², Sien Ng¹, Tisita Das³, Jyotibdha Acharya⁴, Rohit Abraham John¹, Divyam Sharma¹, Putu Andhita Dananjaya⁵, Metikoti Jagadeeswararao², Naveen Tiwari¹, Mohit Ramesh Chandra Kulkarni¹, Wen Siang Lew⁵, Sudip Chakraborty^{3*}, Arindam Basu⁶, Nripan Mathews^{1, 2*}

¹School of Materials Science & Engineering, Nanyang Technological University, Singapore 639798.

²Energy Research Institute @ NTU (ERI@N), Nanyang Technological University, Singapore 637553.

³Materials Theory for Energy Scavenging (MATES) Lab, Harish-Chandra Research Institute(HRI) Allahabad, HBNI, Chhatnag Road, Jhansi, Prayagraj (Allahabad) 211019, India.

⁴School of Electrical and Electronic Engineering, Nanyang Technological University, Singapore 639798.

⁵School of Physical and Mathematical Sciences, Nanyang Technological University, Singapore.

⁶Department of Electrical Engineering, City University of Hong Kong, Hong Kong.

*Corresponding author

Dr. Sujaya Kumar Vishwanath (Email: sujayav@iisc.ac.in)

Dr. Sudip Chakraborty (Email: sudiphys@gmail.com)

Assoc. Prof. Nripan Mathews (Email: nripan@ntu.edu.sg)

Keywords: one dimensional halide perovskites, crossbar memristors, artificial synapses, analog programming, neuromorphic computing

SI Note-1: Experimental Section

(Propyl)pyridinium iodide (PrPyrI) and (benzyl)pyridinium iodide (BnzPyrI): Stoichiometric amounts of pyridine and iodopropane or α -iodotoluene were transferred to a flamed-dry two-neck round bottom flask. The residual moisture or oxygen were removed by introducing a vacuum-nitrogen cycle for three times. Dry acetonitrile (dried with CaH_2 before distillation) was accordingly added into the reaction medium before the resulting mixture was brought to reflux while stirring for 1-2 days, until reaction was complete. This was assessed by ^1H NMR spectroscopy. Upon cooling, the precipitate formed during reaction was isolated by filtration, thoroughly washed with diethyl ether, and dried under vacuum to give a yellow powder.

Growth of single crystals of hybrid 1D materials (PrPyr)[PbI₃] and (BnzPyr)[PbI₃]: Initially, stoichiometric amounts of PbI_2 and PrPyrI or BnzPyrI in DMSO were prepared in small vials and transferred into bigger vials containing antisolvent acetone. 1D perovskite single crystals thus formed by vapor diffusion method, were then filtered and dried for X-ray crystallographic characterization and device fabrication.

Device Fabrication: Commercial Indium tin oxide (ITO) glasses were ultrasonically cleaned with acetone, ethanol and isopropanol (IPA) for 15 mins each. This was followed by 15 mins of UV-ozone treatment. PEDOT:PSS (4086) was first spin-coated at 4000 rpm for 80 s on top of ITO glass (bottom electrode) and annealed for 10 mins at 110 °C. The (PrPyr)[PbI₃] or (BnzPyr)[PbI₃] solution was next spin-coated at 4000 rpm for 30 s on top of PEDOT: PSS and baked on a hot plate for 5 mins at 100 °C. A thin poly (methyl methacrylate) (PMMA) film was finally spin-coated at 4000 rpm for 40 s on top of perovskite. PEDOT: PSS served as a good adhesion layer for the 1D HPs thin films, while PMMA protected it from oxygen and moisture. To complete the device structure, Ag top electrodes were thermally evaporated with a shadow mask (100 μm \times 100 μm) under vacuum (10^{-6} torr).

Computational Methodology

We have performed ion migration calculations based on the electronic structure theory using Vienna *ab-initio* simulation package (VASP)¹ integrated with projected-augmented-wave (PAW)² method of the density functional theory formalism (DFT)^{3, 4}. Throughout the calculations, we have used generalized gradient approximation (GGA) based exchange and correlation functional as implemented in Perdew- Burke-Ernzerhof (PBE) functional⁵. We have considered the plane wave basis set with 500 eV kinetic energy cut-off and 3x3x3 Monkhorst-

Pack k-points for Brillouin zone samplings⁶. After obtaining the fully relaxed structure of iodoplumbate chains in (PrPyr)[PbI₃], we have systematically determined the ion-migration mechanism. All the structures were completely relaxed while achieving the minimum-energy criteria until the Hellman-Feynman force becomes less than 0.01 eV/Å. For determining the transition pathways corresponding to activation energy barrier for halide migration, we have used Nudged Elastic Band (NEB) approach⁷.

Characterizations: Field emission scanning electron microscopy (FESEM, JEOL JSM-7600F) was employed to characterize the topographical and cross-sectional images of the 1D HP memristor. Glancing-angle X-ray diffraction measurements were conducted using a Bruker AXS D8 ADVANCE system with Cu K α radiation ($\lambda = 1.5418\text{\AA}$). The GAXRD spectra were recorded with an incident angle of 5°, a step size of 0.05°, and a delay time of 1s for each step. All electrical measurements were carried out using Keithley 4200 semiconductor parameter analyzer and a vacuum probe station. For X-ray crystallography, single crystals were mounted on a Bruker X8 Quest CPAD area detector diffractometer and data were collected using a I μ S 3.0 Microfocus Mo-K α radiation source ($\lambda = 0.71073\text{\AA}$), at cryogenic temperatures (100 K). Data reduction and absorption corrections were performed using the SAINT and SADABS software packages, respectively⁸. All structures were solved by direct methods and refined by full-matrix least squares procedures on F², using the Bruker SHELXTL-2014 software package^{9, 10}. Non-hydrogen atoms were anisotropically refined, after which hydrogen atoms were introduced at calculated positions and the data was further refined. The graphical illustrations of crystal structures used throughout the main paper and supporting information were created using the program VESTA¹¹.

Physical Characterizations:

Table T1 Crystallographic and structure refinement data for (PrPyr)[PbI₃] and (BnzPyr)[PbI₃].^a

	(PrPyr)[PbI ₃]	(BnzPyr)[PbI ₃]
Empirical formula	C ₈ H ₁₂ I ₃ NPb	C ₁₂ H ₁₂ I ₃ NPb
Formula weight	710.08 g/mol	758.12 g/mol
Temperature	253(2) K	296(2) K
Wavelength	0.71073 Å	0.71073 Å
Crystal size	0.160 x 0.280 x 0.360 mm	0.010 x 0.020 x 0.120 mm
Crystal habit	yellow block	yellow needle
Crystal system	orthorhombic	monoclinic

Space group	P n m a	P 1 21/m 1
	a = 8.1205(4) Å	a = 11.7951(11) Å
	$\alpha = 90^\circ$	$\alpha = 90^\circ$
Unit cell dimensions	b = 9.2677(4) Å	b = 7.8822(7) Å
	$\beta = 90^\circ$	$\beta = 101.304(2)^\circ$
	c = 19.9344(8) Å	c = 11.8001(11) Å
	$\gamma = 90^\circ$	$\gamma = 90^\circ$
Volume	1500.23(12) Å ³	1075.79(17) Å ³
Z	4	2
Density	3.144 g/cm ³	2.340 g/cm ³
Absorption coefficient	17.386 mm ⁻¹	12.132 mm ⁻¹
F(000)	1232	664
Theta range for data collection	2.04 to 31.07°	2.72 to 32.65°
Reflections collected	35801	20470
Coverage of independent reflections	100.00%	99.8%
Absorption correction	Multi-Scan	Multi-Scan
Max. and min. transmission	0.1670 and 0.0620	0.8880 and 0.3240
Function minimized	$\Sigma w(F_o^2 - F_c^2)^2$	$\Sigma w(F_o^2 - F_c^2)^2$
Data / restraints / parameters	2530 / 0 / 72	4177 / 261 / 118
Goodness-of-fit on F ²	1.096	1.028
Δ/σ_{max}	0.001	0.001
Final R indices	1971 data	1976 data
[I > 2 σ (I)]	R1 = 0.0505, wR2 = 0.1208	R1 = 0.0554, wR2 = 0.1416
R indices [all data]	R1 = 0.0667, wR2 = 0.1347	R1 = 0.1407, wR2 = 0.1769
Largest diff. peak and hole	3.158 and -2.473 eÅ ⁻³	1.619 and -1.151 eÅ ⁻³
R.M.S. deviation from mean	0.322 eÅ ⁻³	0.239 eÅ ⁻³

$^{\alpha}R = \Sigma ||F_o| - |F_c|| / \Sigma |F_o|$, $wR = {}^{11/2}$ and (PrPyr)[PbI₃], $w = 1/[\sigma^2(F_o^2) + (0.0506P)^2 + 8.5448P]$; (BnzPyr)[PbI₃], $w = 1/[\sigma^2(F_o^2) + (0.0816P)^2 + 0.1230P]$ where $P = (F_o^2 + 2F_c^2)/3$.

Table T2 Summary of distortion parameters of (PrPyr)[PbI₃] and (BnzPyr)[PbI₃].

No.	Compound	λ_{oct}^{α}	$\sigma_{oct}^{2\beta}$	$\Delta d (x10^{-4})^{\gamma}$
1.	(PrPyr)[PbI ₃]	1.0108	36.14	7.88
2.	(BnzPyr)[PbI ₃]	1.0046	16.68	0.16

$^{\alpha}$ Octahedral elongation (λ_{oct}), $^{\beta}$ octahedral angle variance (σ_{oct}^2), and $^{\gamma}$ octahedral bond length distortion (Δ_{oct}). The equations for each parameter and an explanation of their meanings are as the followings:

$$\text{Octahedral elongation}^{12, 13}: \lambda_{oct} = \frac{1}{6} \sum_{i=1}^6 \left[\frac{d_i}{d_0} \right]^2 \quad (1)$$

$$\text{Octahedral angle variance}^{12-15}: \sigma_{oct}^2 = \frac{1}{11} \sum_{i=1}^{12} (\alpha_i - 90)^2 \quad (2)$$

$$\text{Bond length distortion}^{14}: \Delta_{oct} = \frac{1}{6} \sum_{i=1}^6 \left[\frac{d_i - d_m}{d_m} \right]^2 \quad (3)$$

where d_i represents Pb–Br bond length, d_m to average bond length, d_0 to center-to-vertex distance of a regular polyhedron of the same volume, and α_i to individual Br–Pb–Br angle. λ_{oct} , σ_{oct}^2 and Δ_{oct} provide a quantitative measure of polyhedral distortion independent of the polyhedron effective size. Crystallographic software, VESTA, was used to calculate the last two structural distortion parameters.

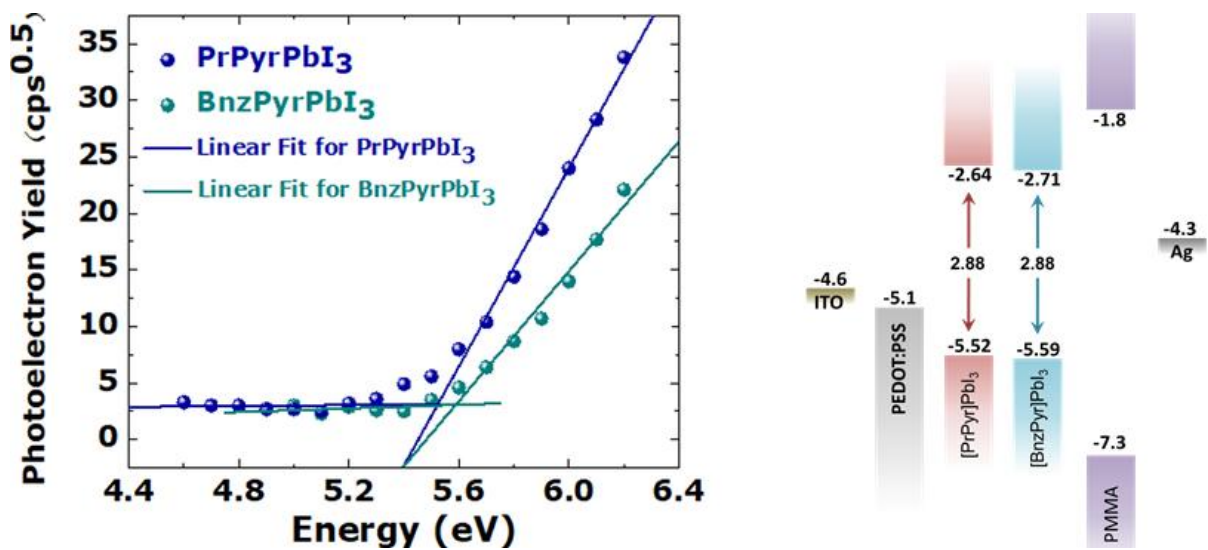


Figure S1 Band gap extraction. (left) Photoelectron spectroscopy in air (PESA) measurements of thin films of (PrPyr)[PbI₃] and (BnzPyr)[PbI₃]. (right) Energy band diagrams of (PrPyr)[PbI₃] and (BnzPyr)[PbI₃] along with the energy levels of the charge transport materials and electrodes comprising the memristor device structure included for reference.

SI Note-2: Benchmarking the memristor performance: Dot-point arrays on a rigid substrate

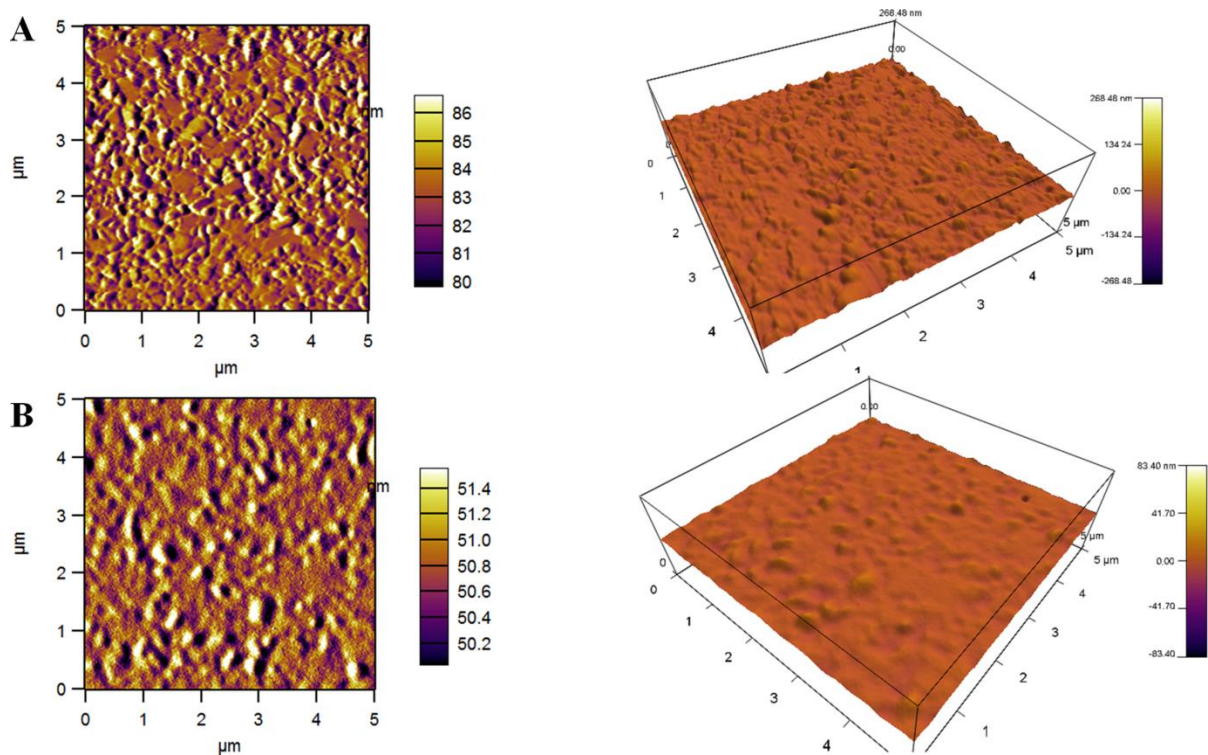


Figure S2 AFM topography images. (A) before and (B) after PMMA coating.

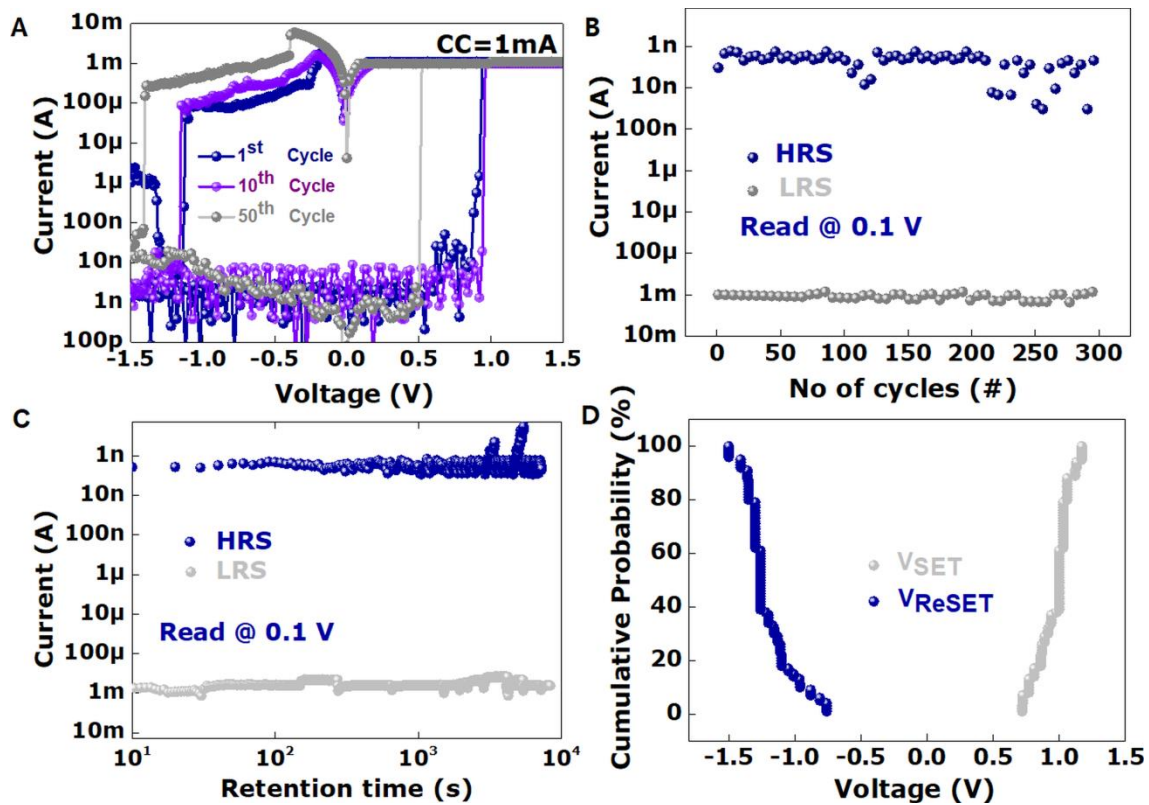


Figure S3 Switching characteristics of rigid (PrPyr)[PbI₃] dot-point memristors. (A)

Representative DC I–V characteristics demonstrating the resistive switching effect in our devices. The voltage sweeps were applied across the top Ag electrode with the bottom ITO electrode grounded. The devices switched (set) seamlessly from its HRS to LRS at $\sim +0.9\text{V}$ when the voltage was swept from $0\text{V} \rightarrow +1.5\text{V} \rightarrow 0\text{V}$. During set, a compliance current of 1mA was applied to prevent the device from hard breakdown. On reversing the polarity $-0\text{V} \rightarrow -1.5\text{V} \rightarrow 0\text{V}$, the device reset back to its initial HRS at $\sim -1.0\text{V}$. This switching behavior remained consistent over the subsequent 50 sweeping cycles, reflecting the excellent stability of the switching process. Test results of (B) AC endurance and (C) retention. (D) Cumulative probability distribution plot of the LRS (light grey) and HRS (blue) across 100 devices.

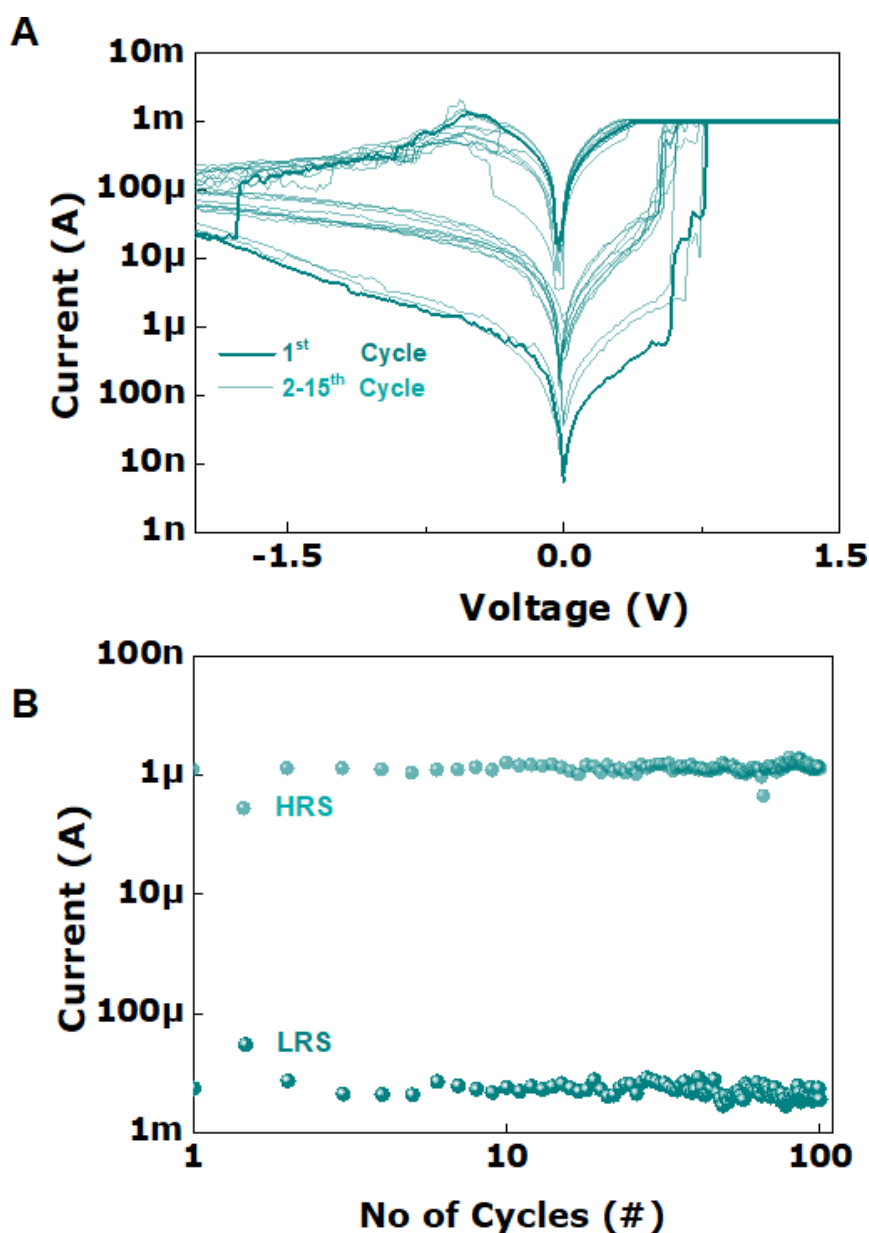


Figure S4 Resistive switching characteristics of BnzPryPbI₃ dot-point memristors. (A)

DC Cycling (B) AC endurance.

SI Note-3: Large-scale flexible dot-point (PrPyr)[PbI₃] memristor array

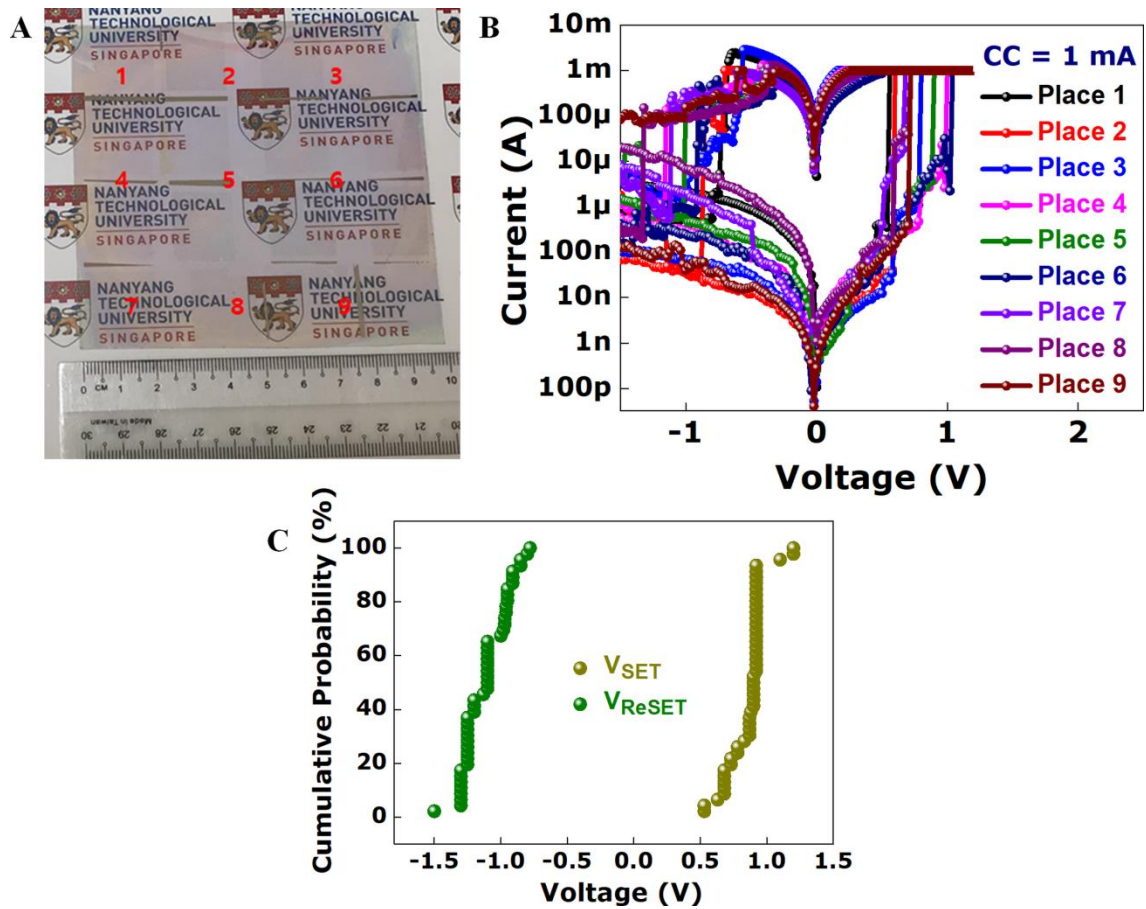


Figure S5 Large-scale flexible dot-point memristor array. (A) Photograph of the flexible dot-point memristor array- Ag/PMMA/PrPyrPbI₃/PEDOT:PSS/ITO-PET. **Switching characteristics** (B) DC I–V characteristics of multiple devices, measured across nine randomly selected locations on the substrate. (C) Cumulative probability distribution plot of the LRS and HRS across 45 devices spread across nine randomly selected locations on the substrate.

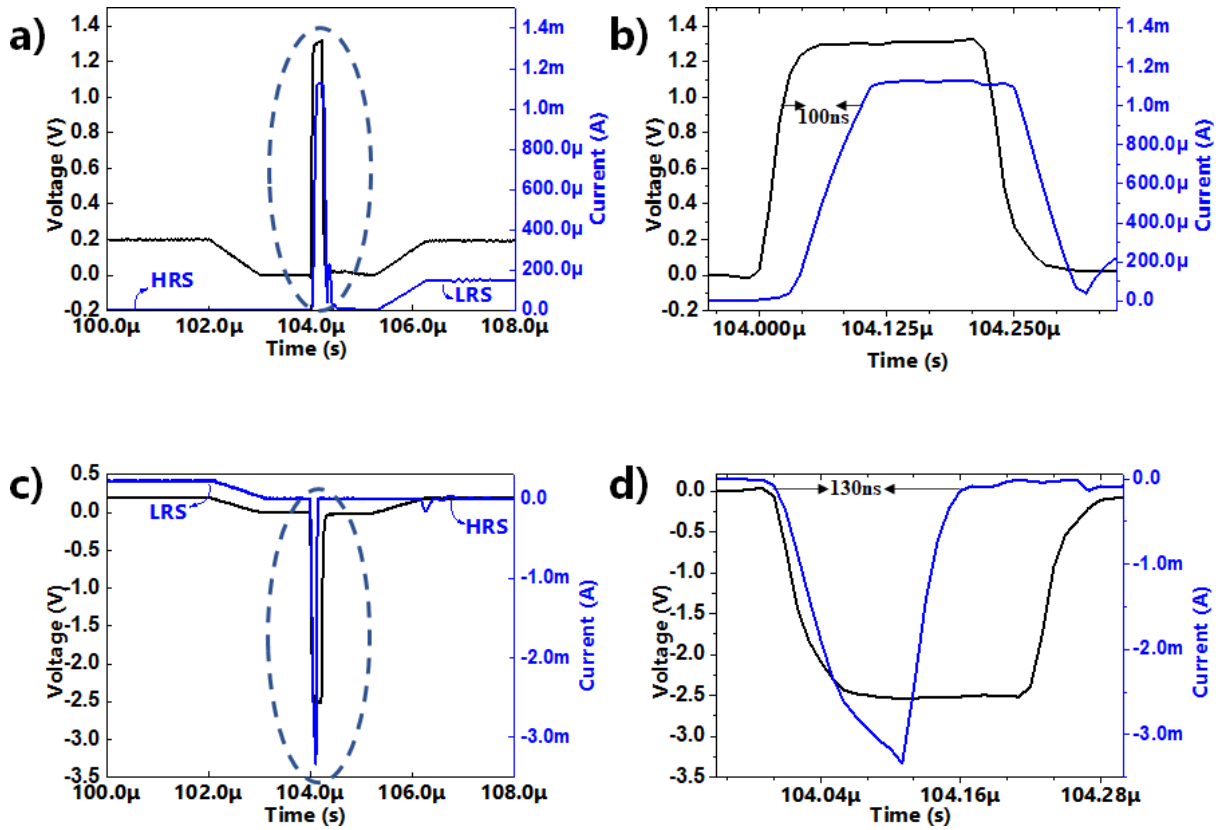


Figure S6: Pulse operation of Ag/PMMA/1D-Perovskite/PEDOTPSS /ITO/PET. a-b) SET, c-d) ReSET

SI Note-4: Comparison of the resistive switching characteristics

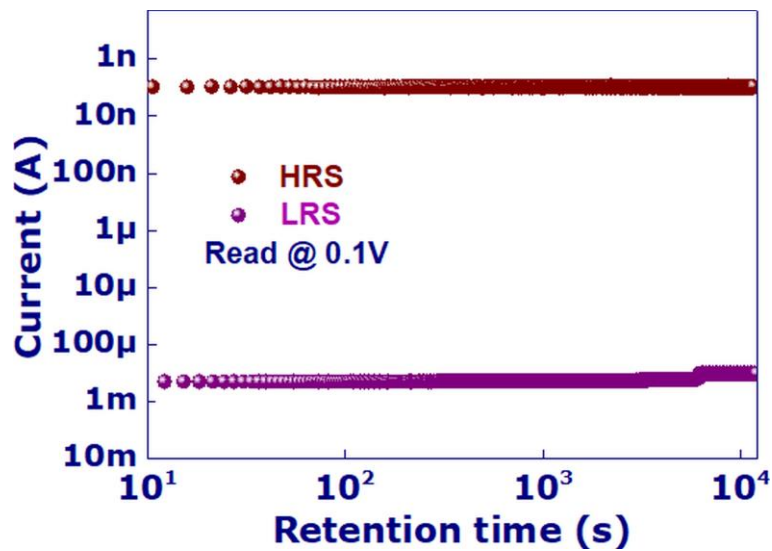


Figure S7. Retention data of flexible crossbar Ag/PMMA/PrPyr(PbI₃)/PEDOT:PSS/Ag/PET devices

Table T3 Summary of the resistive switching characteristics of 1D-(PrPyr)PbI₃ memristors

Device	On/Off ratio	Endurance (no of cycles)	Retention (s)
Dot-point devices on glass substrate	10 ⁵	~300	8500
Dot-point flexible devices	10 ⁵	2000	>10 ⁵
Crossbar flexible devices	10 ⁴ -10 ⁶	450	>10 ⁴

SI Note-5: Intermediate states and Resistive Switching mechanism

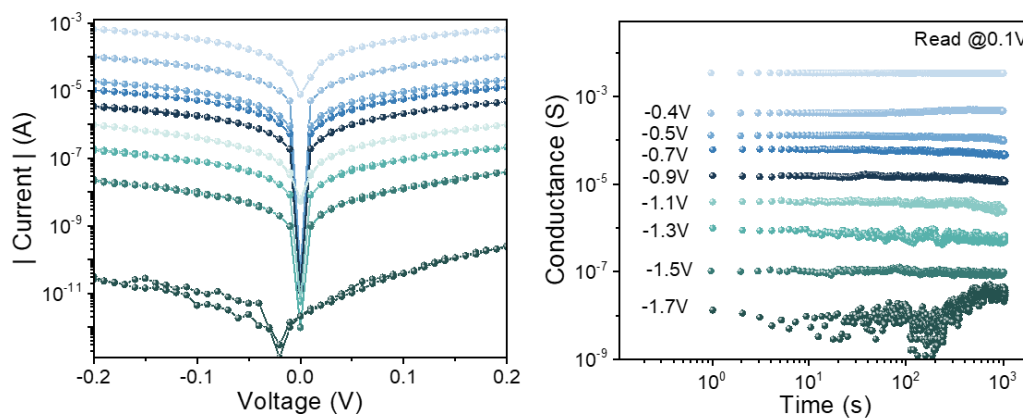


Figure S8 Retention characteristics for multiple resistance states

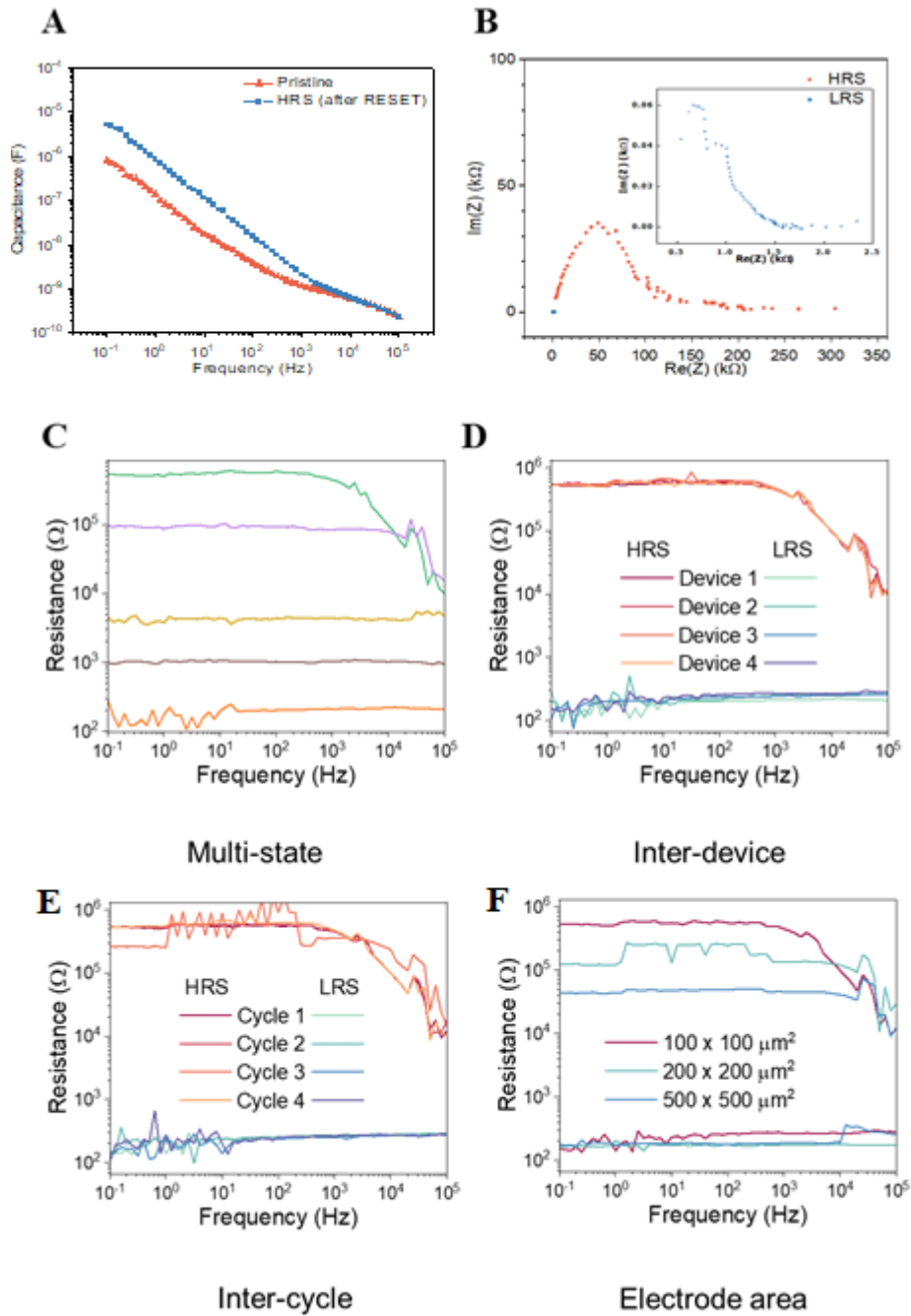


Figure S9 Electrochemical impedance spectroscopy with Bode plot comparison of (A) capacitance at various resistance states (B) Nyquist plot (C) Multi-state (D) Inter-device (E) Inter-cycle (F) Electrode area.

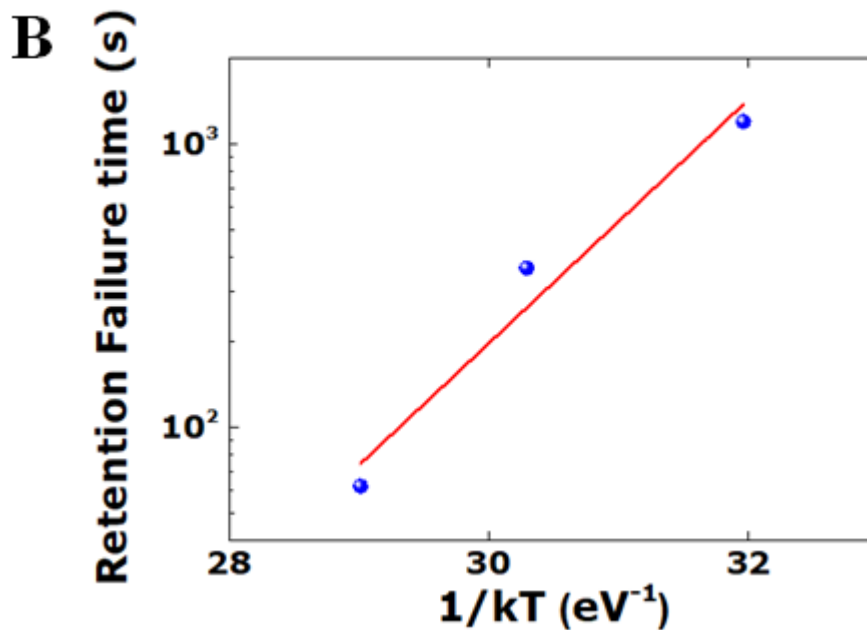
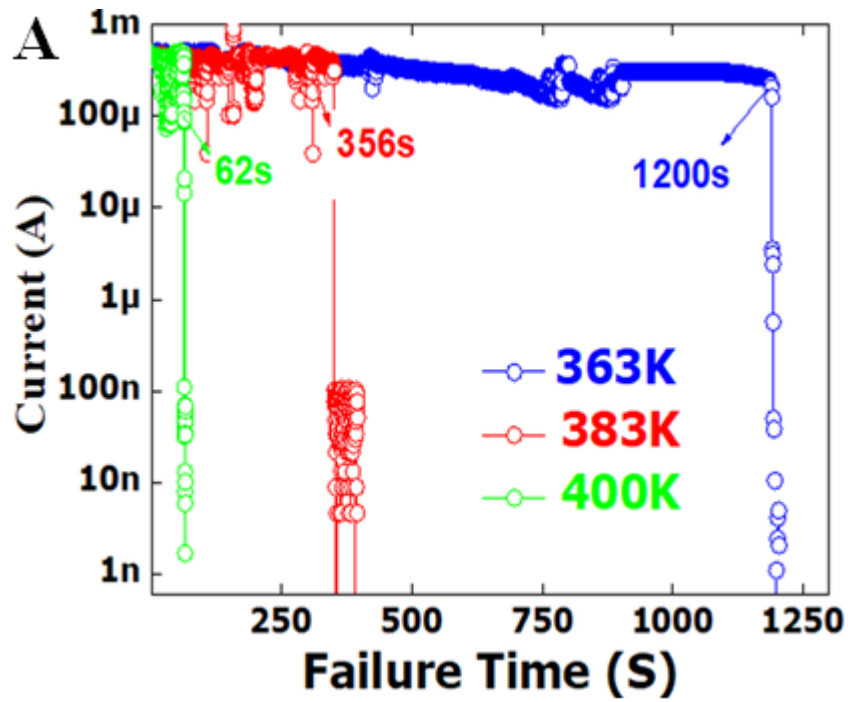


Figure S10 Temperature-dependent LRS retention behaviour of (PrPyr)PbI₃ memristors.

a) Temperature-dependent LRS retention behaviour. The device was set to an initial resistance of $\sim 383\Omega$. A constant read bias (0.1V) was applied to monitor the evolution of device resistance over and b) $\text{time} \ln(t) - 1/kT$ plot.

Resistive switching with Au as top electrode:

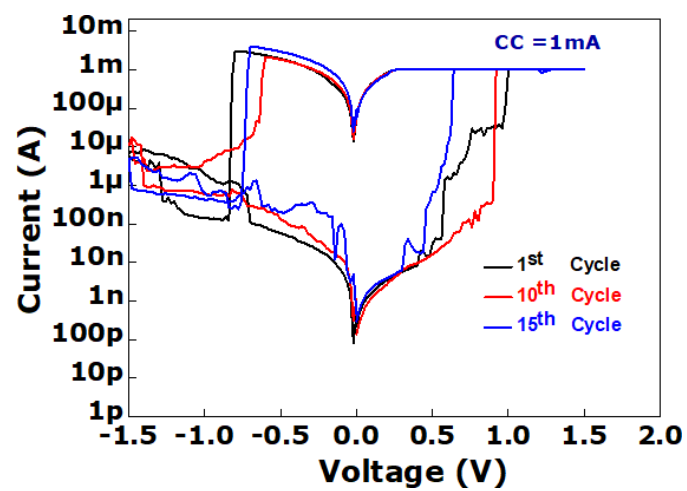


Figure S11 Resistive switching in Au/PMMA/PrPryPbI₃/PEDOT:PSS/ITO/PET

SI Note-6: Neuromorphic Characterization

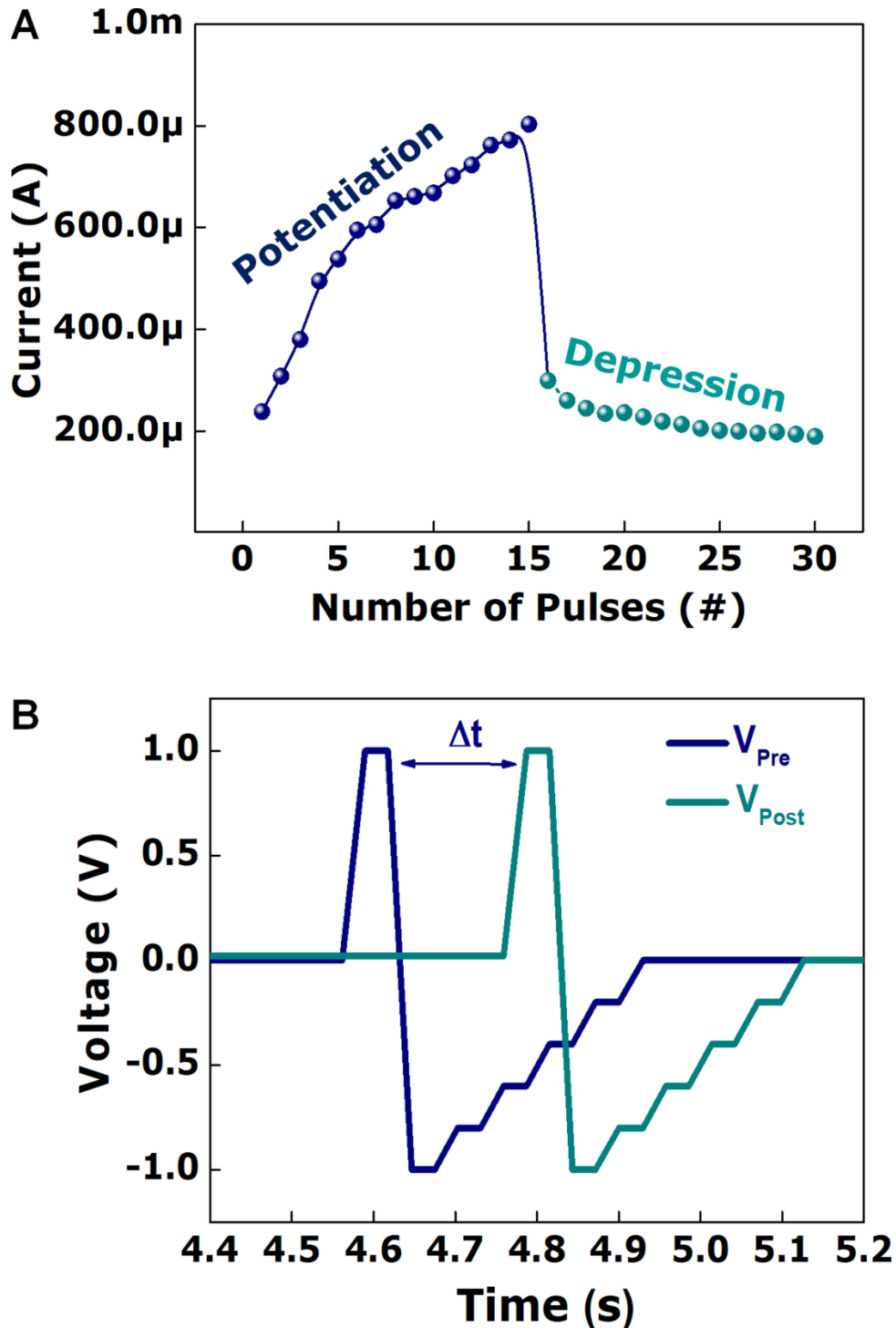


Figure S12 Long-term Plasticity and Spike-timing-dependent plasticity (STDP). (A) Traces of long-term potentiation and depression induced via blind programming pulses (+1V for LTP and -1V for LTD, pulse width=10ms). (B) Input waveforms applied at the pre and post-

synaptic terminals to realize antisymmetric Hebbian learning rules in (PrPyr)[PbI₃] synapses.

Repeated arrival of pre-post or post-pre spike pairs lead to resistance changes above the threshold for non-volatile conductance change in proportion to the voltage and time-integrated device conductance function ($f(V_{\text{pre}}-V_{\text{post}}, t)$), where the net voltage on the device at each instant of time (t) is defined by the voltage difference between the pre- and post-spike ($V_{\text{pre}}-V_{\text{post}}$)^{16, 17}. Changes in conductance were compared to the initial conductance value to convert the data to percentage weight changes (reading pulses of 0.02V was utilized for this measurement). The device was then allowed to relax back or erased to the initial conductance state before the next measurement to avoid dependence of previous history. For example, an interval ($t_{\text{post-pre}}$) of +20ms resulted in a net voltage of $V_{\text{pre}-V_{\text{post}}} = (+1.0) - (-1.0) = +2.0\text{V}$ developed across the device, triggering a permanent increase in the channel conductance or LTP (~98%). On arrival of presynaptic pulses after postsynaptic pulses, i.e. $t_{\text{post-pre}}$ of -20ms, the maximum net voltage developed across the device was $V_{\text{pre}-V_{\text{post}}} = (-1.0) - (+1.0) = -2\text{V}$ and this resulted in a decrease in conductance or LTD (~-56%). These measurements were repeated for several combinations of spike intervals and the weight changes were plotted as a function of $t_{\text{post-pre}}$ as shown in **Figure 4A**. Weight changes were predominant at small pulse intervals, and weakened with increase in the interval, reflecting strong temporal correlations between the pre- and post-synaptic spikes¹⁶.

SI Note-6: SNN simulation with STDP synapses for handwritten digit recognition:

The architecture of the SNN used for handwritten digit recognition is shown in **Figure 5A**. The network is trained on handwritten digits from MNIST dataset. The dataset contains digits 0-9 as 28×28-pixel images. The task is classifying the images into 10 classes. The images were first converted to Poisson spike trains using rate encoding. The firing rate of the spike train corresponding to each pixel is proportional to the intensity of the pixel. The input spike trains are connected to the excitatory neurons through HP-synapses that learn the input patterns through STDP. Each of the excitatory neuron is connected to one inhibitory neuron and each inhibitory neuron is connected to all excitatory neurons except the one from which it accepts the connection. Whenever an excitatory neuron spikes, it triggers the inhibitory neuron to spike which in turn inhibits all other excitatory neurons from spiking. The neurons are modelled as leaky-integrate-and-fire (LIF) neurons with neuron dynamics defined as:

$$\tau_m \frac{dV}{dt} = -(V - V_{reset}) + RI(t) \quad (4)$$

where $V(t)$ and V_{reset} are the membrane potential and reset potential, $I(t)$ is the total input synaptic current, R is the membrane resistance and τ_m is the membrane time constant. The neuron spikes when $V(t) > V_{Threshold}$ then resets. The synaptic current kernel is modelled as an exponentially decaying function and dynamics of the synaptic conductance is governed by:

$$\tau_g \frac{dg}{dt} = -g \quad (5)$$

Where g is the synaptic conductance and τ_g is the synaptic time constant. The conductance decays in absence of any pre-synaptic spikes and increases instantaneously whenever there is a pre-synaptic spike, The synaptic current is given by:

$$I(t) = W \times g \times a \quad (6)$$

Where W is the synaptic weight and a is a constant scaling factor. The HP synapses are initialized to random weights and learn the input patterns through STDP.

The weight change ΔW is calculated at each post-synaptic spike according to STDP rule:

$$\Delta W = (X_{pre}(t_{post}) - X_{tar})(W_{max} - W)^\mu \quad (7)$$

Where $X_{pre}(t)$ is the pre-synaptic trace that mimics the temporal dynamics of pre-synaptic current. It increases by one instantaneously whenever an input spike is presented and decays exponentially otherwise. The variable X_{tar} represents the target value of pre-synaptic trace at the time of post-synaptic spike. If an input neuron spikes rarely, this X_{tar} factor ensures that the synaptic weight of the corresponding synapse decreases, and the neuron eventually disconnects. The effect of this parameter is similar to using standard STDP with random noise added to the inputs¹². The final weight scaling factor ensures that the weights are upper bound by W_{max} and the μ parameter determines the dependence of current weight update on previous weight. To emulate the hardware constraints of the HP memristor synapses, the same voltage waveform is used for both STDP and post-synaptic current kernel.

The connections between excitatory and inhibitory neurons have fixed weights and the lateral inhibition resulting from the connection excitatory and inhibitory neurons result in a competition between excitatory neurons. To ensure fair participation of all the neurons in this competition, a threshold adaptation strategy is also incorporated in excitatory neurons, whereby the spiking threshold of a neuron increases instantaneously each time it spikes and decays exponentially otherwise. As a result of this winner-take-all competition coupled with the STDP

weight learning in input to excitatory synaptic connections, the receptive fields of each excitatory neurons start resembling one of the possible input patterns. Whenever an excitatory neuron spikes for a specific input pattern, its receptive field more closely resembles the corresponding input pattern. **Figure 5C** shows this evolution of receptive fields through the training process. In **Figure 5D**, we show that the classification accuracy indeed improves when more and more training patterns are sent to the network resulting in receptive fields with more accurate and diverse representations of input patterns. Finally, while **Figure 5D** shows increase in accuracy with increasing number of training samples, passing the same training samples multiple times also result in increased classification accuracy. This is evident from **Figure S8** where the network is trained on the same 6000 training samples for multiple epochs and the accuracy increases by $\sim 3.5\%$ after 10 epochs.

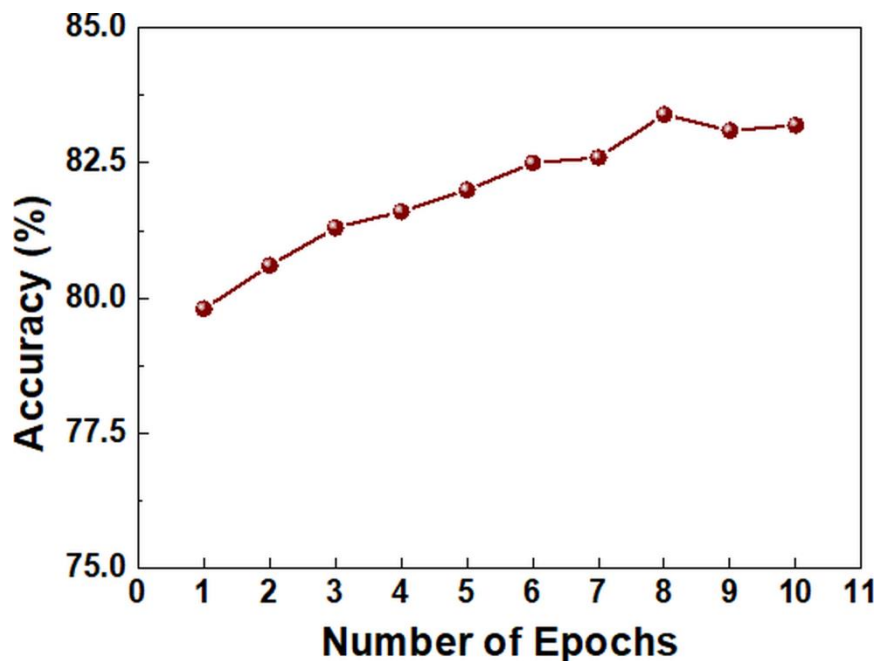


Figure S13 SNN training for multiple epochs. The network have trained for multiple epoches with 6000 training samples and tested on 1000 testing samples. The classification accuracy increases from 79.8% at the first epoch to $>83\%$ after 10 epoches.

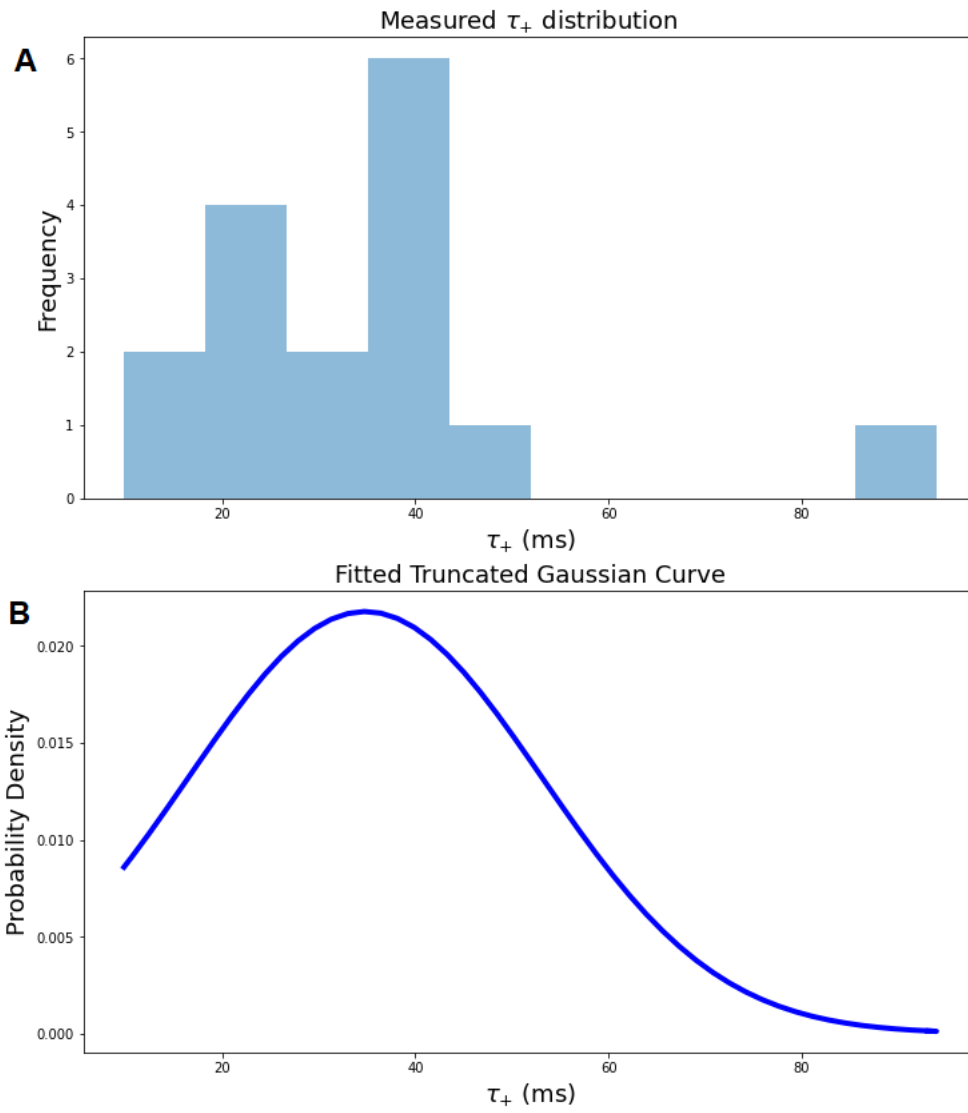


Fig S14: Histogram of measured τ_+ values for 16 synapses (A) and the truncated Gaussian curve fitted over the distribution (B).

SI Note-7: Comparison with literature

Table T4 Comparison of the switching characteristics of our devices with literature.

Structure	Set/Reset voltage (V)	ON/OFF Ratio	Endurance (cycles)	Retention (s)	No. of Bending Cycles / Bending radius (cm)	Ref
Al/CsPbBr ₃ /PEDOT:PSS/ITO/PET	-0.6/1.7	10 ²	50	—	100 / --	18
Au/Cs ₃ Bi ₂ I ₉ /ITO/PET	0.3/-0.5	10 ²	1000	—	100 / 0.9	19
Ag/CsPbBr ₃ /PEDOT:PSS/ITO/PET	1.5/-1.5	10	300	—	50 / --	20
Ag/CsPbBr ₃ /MoO ₃ /Ag/PET*	1/-2	10 ²	50	—	50 /	21
Graphene/2D (PEA) ₂ PbBr ₄ (single crystal)/Au	2.8/—	10 ²	100	10 ³	—	22
Ag/PMMA/(BzA) ₂ CuBr ₄ /Pt	0.2/-0.3	10 ⁸	2000	10 ³	—	23
Au/MAPbI _{3-x} Cl _x /FTO	0.1/-0.4 5	10 ⁴	400	10 ⁴	—	24
Al/(3AMP)PbI ₄ /ITO	0.6/-2	10 ³	1000	10 ³	—	25
Ag/CsPb _{1-x} BixI ₃ /ITO	4/-3.6	~10	500	10 ⁴	—	26
Au/MAPbI ₃ /Pt	1/-1	10 ⁴	500	10 ⁵	—	27
Au/MAPbI ₃ /Pt*	0.6/~ 0.7	10			—	27
Al/CH ₃ NH ₃ PbBr ₃ NPs:PEO/Al*	10/-10	10 ⁴		10 ⁴	—	28
Ag/CsPbBr ₃ /pTPD/PEDOT:PS/ITO	5/-7	10 ³	5655	10 ⁵	—	29
Ag/PMMA/PrPyr(PbI ₃)/PEDOT:PSS/ITO/PET	0.9/-1	10 ⁵	2000	10 ⁵	300 / 1.5	This work

Ag/PMMA/PrPyr(PbI ₃)/PEDO	0.96/-	10 ⁴ -10 ⁶	500	10 ⁴	Bendable	This
T:PSS/Ag/PET*	1.21					work

* denotes crossbar configuration

References:

1. G. Kresse and J. Furthmüller, *Phys Rev B Condens Matter*, 1996, **54**, 11169-11186.
2. P. E. Blöchl, *Phys Rev B Condens Matter*, 1994, **50**, 17953-17979.
3. P. Hohenberg and W. Kohn, *Physical review*, 1964, **136**, B864.
4. W. Kohn and L. J. Sham, *Physical review*, 1965, **140**, A1133.
5. J. P. Perdew, K. Burke and M. Ernzerhof, *Physical review letters*, 1996, **77**, 3865.
6. H. J. Monkhorst and J. D. Pack, *Physical review B*, 1976, **13**, 5188.
7. G. Henkelman and H. Jónsson, *The Journal of chemical physics*, 2000, **113**, 9978-9985.
8. S.-P. APEX, *Madison, Wisconsin, USA*.
9. G. Sheldrick, *Program for crystal structure refinement*, 1997.
10. G. M. Sheldrick, *Acta Crystallographica Section A: Foundations of Crystallography*, 2008, **64**, 112-122.
11. K. Momma and F. Izumi, 2006.
12. K. Robinson, G. Gibbs and P. Ribbe, *Science*, 1971, **172**, 567-570.
13. N. W. Thomas, *Acta Crystallographica Section B: Structural Science*, 1989, **45**, 337-344.
14. A. Ertl, J. M. Hughes, F. Pertlik, F. F. Foit Jr, S. E. Wright, F. Brandstätter and B. Marler, *The Canadian Mineralogist*, 2002, **40**, 153-162.
15. M. Fleet, *Mineralogical magazine*, 1976, **40**, 531-533.
16. R. A. John, N. Yantara, Y. F. Ng, G. Narasimman, E. Mosconi, D. Meggiolaro, M. R. Kulkarni, P. K. Gopalakrishnan, C. A. Nguyen and F. J. A. M. De Angelis, 2018, **30**, 1805454.
17. R. A. John, N. Yantara, S. E. Ng, M. I. B. Patdillah, M. R. Kulkarni, N. F. Jamaludin, J. Basu, n. Ankit, S. G. Mhaisalkar and A. Basu, *Advanced Materials*, 2021, **33**, 2007851.
18. D. Liu, Q. Lin, Z. Zang, M. Wang, P. Wangyang, X. Tang, M. Zhou and W. Hu, *ACS applied materials & interfaces*, 2017, **9**, 6171-6176.
19. Y. Hu, S. Zhang, X. Miao, L. Su, F. Bai, T. Qiu, J. Liu and G. Yuan, *Advanced Materials Interfaces*, 2017, **4**, 1700131.
20. Q. Lin, W. Hu, Z. Zang, M. Zhou, J. Du, M. Wang, S. Han and X. Tang, *Advanced Electronic Materials*, 2018, **4**, 1700596.
21. C. Zou, L. He and L. Y. Lin, *physica status solidi (RRL)–Rapid Research Letters*, 2019, **13**, 1900182.
22. H. Tian, L. Zhao, X. Wang, Y.-W. Yeh, N. Yao, B. P. Rand and T.-L. Ren, *Acs Nano*, 2017, **11**, 12247-12256.
23. S. Y. Kim, J. M. Yang, E. S. Choi and N. G. Park, *Advanced Functional Materials*, 2020, **30**, 2002653.
24. F. Zhou, Y. Liu, X. Shen, M. Wang, F. Yuan and Y. Chai, *Advanced Functional Materials*, 2018, **28**, 1800080.
25. Y. Park and J.-S. Lee, *ACS Applied Materials & Interfaces*, 2022, **14**, 4371-4377.
26. S. Ge, Y. Wang, Z. Xiang and Y. Cui, *ACS applied materials & interfaces*, 2018, **10**, 24620-24626.
27. B. Hwang and J. S. Lee, *Advanced Materials*, 2017, **29**, 1701048.
28. E. Ercan, J. Y. Chen, P. C. Tsai, J. Y. Lam, S. C. W. Huang, C. C. Chueh and W. C. Chen,

- Advanced Electronic Materials*, 2017, **3**, 1700344.
29. R. A. John, Y. Demirađ, Y. Shynkarenko, Y. Berezovska, N. Ohannessian, M. Payvand, P. Zeng, M. I. Bodnarchuk, F. Krumeich and G. Kara, *Nature communications*, 2022, **13**, 2074.